CrossMark

Theoretical and experimental investigations of intermediate bands in ZnS–Mg nanocrystalline thin film photosensor

Avinash S. Dive[1] · Nanasaheb P. Huse[1] · Ketan P. Gattu[2] · Ravikiran B. Birajdar[1] ·
Devesh R. Upadhyay[3] · Ramphal Sharma[1,2]

Abstract The electronic structure of ZnS and Mg-doped ZnS thin films were calculated by first principle investigation within the density functional theory. For experimental analysis, the ZnS and Mg–ZnS samples were grown by simple one step, chemical bath deposition on a glass substrates. The electronic structure reveals the systematic formation of the intermediate band through Mg substitution in wurtzite ZnS at zinc site. This result is well correlated with the experimental results. The structural results obtained from X-ray diffraction study showed hexagonal wurtzite crystal structure with average crystallite size 23 and 21 nm for ZnS and Mg–ZnS respectively. It is observed from UV–Vis spectra that the energy band gap decreases with Mg content due to the creation of new intermediate bands in the band gap region. Raman spectra obtained from the pure and Mg–ZnS films exhibit the longitudinal optical phonon modes. Photosensing properties of the as-grown ZnS and Mg–ZnS thin films were studied by I-V measurements, the photosensitivity was found to be 92 and 96% respectively.

✉ Ramphal Sharma
  rps.phy@gmail.com

1 Thin Film and Nanotechnology Laboratory, Department
   of Physics, Dr. Babasaheb Ambedkar Marathwada
   University, Aurangabad 431004, India

2 Department of Nanotechnology, Dr. Babasaheb Ambedkar
   Marathwada University, Aurangabad 431004, India

3 SRM University, Srm Nagar, Kancheepuram District,
   Kattankulathur, Tamil Nadu 603 203, India

1 Introduction

Presently, many researchers are focusing towards increasing the conversion efficiency of the optoelectronic devices as well as the performance of photovoltaic solar cells. With this aim intermediate band (IB) materials are playing a major role. Before that in a solar cell, there is a direct transition from valence band (VB) to the conduction band (CB) but in the case of IB materials, new bands introduce in actual band gap [1]. Thus the transition of electrons from VB to CB not only occurs from higher energy photons than the band gap energy but also from couple of low energy photons. IB's provides a comprehensive response to the solar spectrum via three optical transitions [2], such as VB to CB, VB to IB and IB to CB [3, 4] shown schematically in Fig. 1. The main focus towards IB's in the manuscript is due to increasing photocurrent with reducing photovoltage which provides good photosensing results. Also only few reports are available on intermediate band solar cells (IBSC's) predicts efficiency up to ~63.1% [5], which is much higher compared to the single junction solar cell (~40.7%) [3, 6]. From the IB, we can get the actual rise in the optical absorbance that can be verified from the theoretical and experimental results. Auxiliary, IB's offers a countless prospect to researcher community for achieving a more simplistic single junction high-efficiency solar cells.

In fact, an IB's can be created through quantum dots or by inserting the suitable impurities into the bulk host semiconductor [7], in which the bulk IB's materials are easy to fabricate than quantum dots [8] and has a stronger absorption due to the higher density of the IB's [9]. Previously, many first principle calculations based on the density functional theory (DFT) have been performed to design and understand the ZnS IB material. It is obvious because of
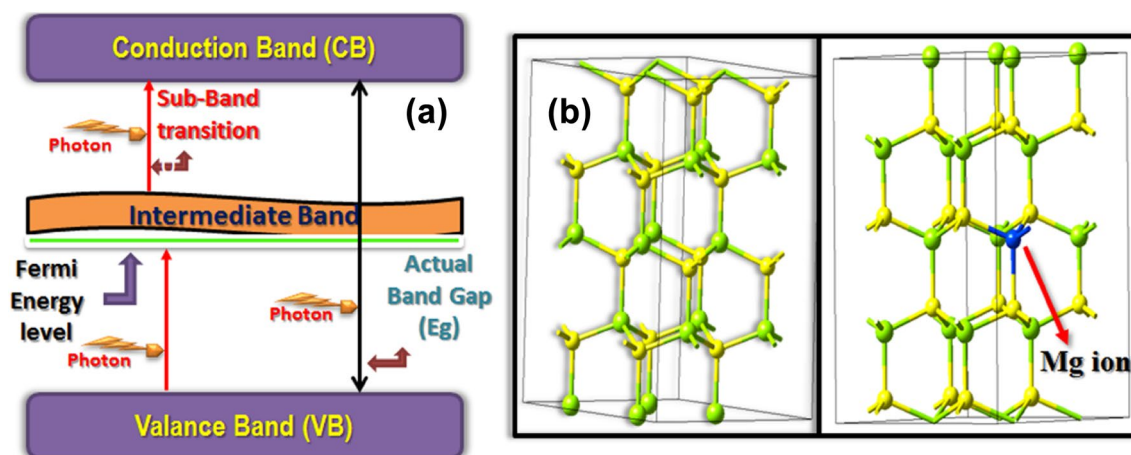
Fig. 1 **a** Schematic bandstructure with intermediate bands. **b** Optimised supercell of ZnS and Mg–ZnS obtained from DFT calculation

Mg doping in ZnS successfully creates IB and the same is reported here.

In this work, we carefully studied the theoretical and experimental optoelectronic properties and photosensing study of ZnS and Mg-doped ZnS thin films. IB were introduced in ZnS by Mg doping to enhance the absorption of solar spectrum greatly and its conversion efficiency [10]. Therefore, one additional absorption peak appears in the absorption spectrum around ~520 nm (~2.38 eV) when ZnS is doped with Mg, arising from the subgap absorptions which is consistent with the theoretical results. Samples were grown by simple one step chemical bath deposition technique on amorphous glass substrate. Further, the films are characterised by X-ray diffraction (XRD), Raman, UV–Vis spectroscopy and I-V characteristics interfaced with solar simulator. Our results clearly demonstrate that the Mg-doped ZnS thin films can be potentially used in the optoelectronic devices or in an IB photovoltaic materials.

2 Experimental details

The nanocrystalline ZnS and Mg–ZnS thin films were synthesized using the simple, one-step chemical bath deposition method. The zinc nitrate hexahydrate $[Zn(NO_3)_2 \cdot 6H_2O]$, magnesium nitrate hexahydrate $[Mg(NO_3)_2 \cdot 6H_2O]$ and thiourea $[CH_4N_2S]$ were used as source materials for deposition of the ZnS as well as Mg–ZnS thin films. Before deposition, the substrates were cleaned by chromic acid, laboline, deionized water and then air-dried. For the deposition of ZnS thin films 0.5 M $Zn(NO_3)_2 \cdot 6H_2O$ and 0.5 M CH_4N_2S were dissolved in 40 ml DI water separately and were stirred for 20 min. Three drops of hydrazine hydrate (80%) [11] were added to Zn source solution. The pH of the Zn source solution

was adjusted to ~11 by dropwise addition of ammonia solution. Further, both the Zn and S precursor solutions were transferred to a 100 ml beaker. The pre-cleaned glass substrates were immersed vertically in the beaker and the beaker was kept in water bath at 50 °C for 1 h. The deposited films were washed with distilled water and dried in air subsequently. The same procedure was followed for the deposition of $Zn_{0.95}Mg_{0.05}S$ thin films, in this case 0.025 M $[Mg(NO_3)_2 \cdot 6H_2O]$ was added as a Mg source to the Zn precursor solution. The synthesized thin films both pure and Mg-doped were found to have light yellowish colour.

The synthesized thin films of ZnS and Mg–ZnS were then characterized for their structural and optoelectronic properties. The XRD patterns were recorded on Bruker AXS, Germany (D8 Advanced) diffractometer in the scanning range 20°–80° using Cukα radiations with wavelength of 1.5405 Å. The electronic transitions in the films were monitored from the optical absorbance spectra recorded in the wavelength range of 300–1100 nm using UV–Vis spectrophotometer Perkin Elmer Lamda-25. The Raman spectra of the samples were recorded using Renishaw in-Via Raman spectrometer (Renishaw, Wotton-under-Edge, UK) at a solution of 0.3 cm^{-1}. Ar$^+$ laser of 532 nm wavelength is used for excitation. The photosensing experiments were recorded by illuminating these nanostructured thin films to 100, 200 and 300 W/cm^2 light source and the data were taken from the computer interfaced with I-V measurement setup KEITHLEY 2400 source meter.

2.1 Computational details

The band structure and total density of states (TODS) calculations using first principles DFT were performed using the MedeA-(VASP) Vienna ab initio simulation package with the plane-wave pseudopotentials. A

$2\times2\times2$ supercell was built with the wurtzite ZnS unit cell with P6$_3$mc as the space group. To study the effect of doping magnesium (Mg) into the ZnS system, one zinc (Zn) atom was replaced with one magnesium (Mg) atom in the supercell to form ~5% doping. Figure 1b shows the optimized supercells of ZnS and Mg–ZnS thin films obtained from DFT calculations. The DFT calculations were performed using generalised gradient approximation (GGA) functional with Perdew-Burke-Ernzerhof (PBE) to describe the electron–electron exchange and correlation effects [12, 13]. The DFT equations were solved via projector augmented wave method using plane wave basis set as implemented in Vienna Ab Initio Simulation Package (VASP) interfaced with MedeA technology platform. The undoped supercell $(ZnS)_{16}$ consist of 16 Zn atoms and 16 S atoms. After incorporation of one Mg atom in ZnS takes the form as $MgZn_{15}S_{16}$. The residual force of 0.01 eV/Å for varying internal position of atoms was used to attain the minimum energy state as well as 400 eV was set as the cutoff kinetic energy. The $2\times2\times2$ K-mesh was used which correspond to spacing <0.5 Å in reciprocal space. Methfessel-Paxton type of smearing was used with smearing width of 0.2 eV. Real space projection operator was used as the system contains a large number of atoms.

3 Results and discussion

3.1 Structural studies

The structural analysis of these ZnS and Mg–ZnS thin films were carried out using the XRD pattern shown in Fig. 2. The XRD pattern reveals that the deposited thin films are composed of fine polycrystalline nanoparticles. The diffraction peaks of Mg–ZnS thin films slightly shifted towards the lower 2Θ angle compared to pure ZnS. The shift of peaks towards the lower diffraction angles marks compressive stress which results in elongation of lattice parameters of the thin films. In wurtzite crystal structure lattice parameters are 'a' and 'c', the lattice constants estimated for both pure and Mg doped ZnS thin films are given in Table 1. The deviation in the lattice constants is because of non-uniform distribution as well as decrease in interatomic spacing [14, 15] after incorporation of Mg^{2+} ions in ZnS lattice and the difference in the ionic radius of Mg^{2+} (0.71 Å) which is smaller than that of Zn^{2+} (0.74 Å) [16, 17]. The effective change in lattice parameters defines the successful incorporation of Mg^{2+} ions in ZnS lattice which consistently follows the Vegard's law [18]. The estimated values were compared with standard JCPDS card given in Table 1. The estimated c/a ratio shows the hexagonal closed packed structure (Table 1). The strain of pure ZnS and Mg–ZnS samples was calculated from XRD data using the Stokes-Wilson relation shown in Eq. (1) implies an increase in strain with Mg substitution [19, 20].
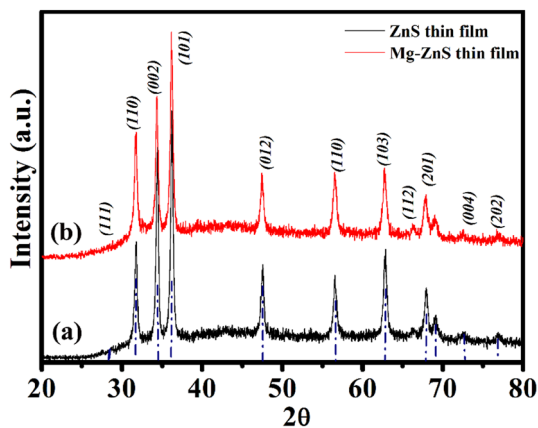
$$\varepsilon = \frac{\beta_{hkl}}{4\tan\theta} \tag{1}$$

$$D = \frac{0.9\lambda}{\beta\cos\theta} \tag{2}$$

where, ε is a strain in the sample and β_{hkl} is the full width at half maximum at angle 2θ. The average crystallite size were estimated using the Scherer equation (2) [19, 21], where λ is the wavelength of X-ray used i.e. 1.5405 Å, β is the FWHM of the peak; θ is the peak position and D is the crystallite size. The average crystallite size for ZnS and Mg–ZnS were found to be 23 nm and 21 nm respectively.
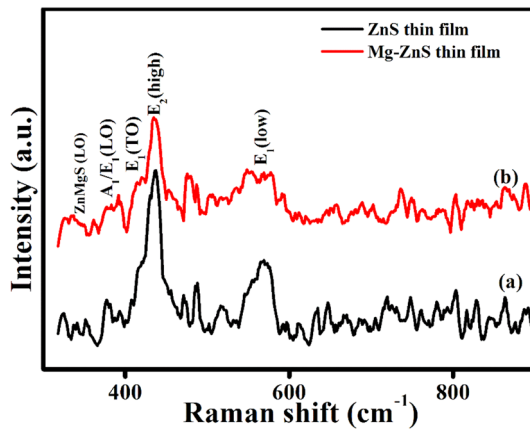

Fig. 2 X-ray diffraction patterns of *a* ZnS and *b* Mg–ZnS thin films

Table 1 Structural parameters of ZnS and Mg–ZnS thin films calculated from XRD data

Sample	Lattice parameters		c/a ratio	Strain	Average crystallite size (nm)	# JCPDS card
	a (Å)	c (Å)				
Wurtzite ZnS	3.64	5.27	1.44	0.004337	23	75-1547
Wurtzite Mg–ZnS	3.66	5.24	1.43	0.004757	20	46-1058

Fig. 3 Raman spectrum of *a* ZnS and *b* Mg–ZnS thin films

Fig. 4 Absorbance spectra of *a* ZnS and *b* Mg–ZnS thin films (*Inset*) Tauc's plot for bandgap determination

3.2 Raman spectrum analysis

The room temperature Raman spectra for the as-grown ZnS and Mg–ZnS thin films are shown in Fig. 3. The CBD grown ZnS and Mg–ZnS thin films confirms the wurtzite crystal structure which belongs to P6$_3$mc space group [22]. The zone-center optical phonons can be classified according to the following irreducible representations, Eq. (3).

$$\Gamma_{opt} = A_1 + E_1 + 2E_2 + 2B_1 \qquad (3)$$

where, A_1 and E_1 modes are polar modes and both are Raman and infrared active, the E_2 modes are nonpolar and Raman active and the B_1 modes are silent modes. The peak at 435 cm^{-1} is characteristic of the wurtzite lattice [23], the sharp peak indicates higher crystalline order. The peak at 356 cm^{-1} is defined for ZnMgS as LO mode. The phonon modes observed at 435 and 573 cm^{-1} can be assigned to E_2(high) and E_1(LO), respectively [24]. Raman peaks other than 573 cm^{-1} observed between 540 and 580 cm^{-1} are associated with structural disorders [25], such as oxygen vacancy and Zn interstitials [26]. The reduction in peak intensities with the Mg doping can be associated with the generated disorders in the crystal. In addition, the second order Raman scattering is seen in between 350 and 450 cm^{-1} which consist of longitudinal optical + transverse acoustic (LO + TA) phonon modes at ~421 and 420 cm^{-1} for pure and Mg–ZnS thin films [24, 27].

3.3 Optical study

Figure 4, represents the optical absorbance spectra of the ZnS and Mg–ZnS thin films recorded as a function of wavelength versus absorbance coefficient. The electronic transitions in the ZnS and the Mg–ZnS thin films can be monitored by studying the absorbance and band gap energy
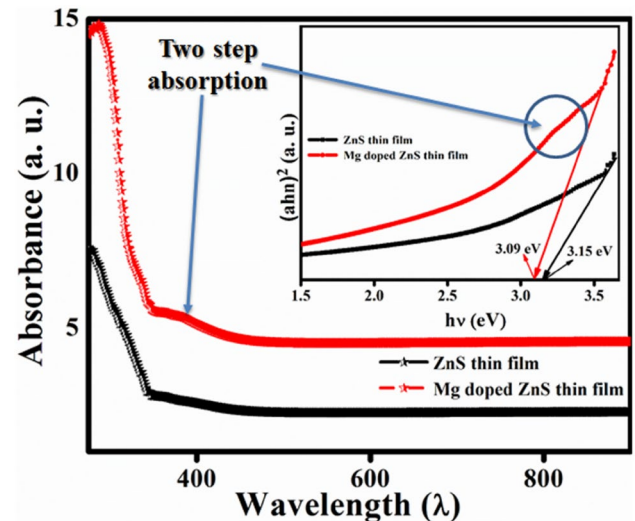
of the materials [28]. The absorbance edges were observed at 390 and 401 nm for the pure and Mg–ZnS thin films respectively. One additional peak observed in the absorption spectrum of Mg–ZnS thin film at 520 nm (2.38 eV) [29]. A shift in absorbance edge towards higher wavelength after Mg addition denotes the clear red shift in energy bandgap. The incorporation of Mg in ZnS lattice creates some new intermediate states in the pure ZnS electron band structure. These IB lie at the centre of the solar spectrum which may enhance the absorption beyond the Shockley-Queisser limitation [30] for solar cells. The formation of IB are also observed in the band structure and density of states obtained from DFT calculations, discussed in the DFT section. This IB allows the extra generation of charge carriers from two-step absorption which is shown in the Fig. 4. The energy band gap was calculated using the Tauc's relation [31, 32], Eq. (4).

$$\alpha h\upsilon = A(h\upsilon - E_g)^n \qquad (4)$$

where α is the absorption coefficient, hυ is the photon energy, A is a band edge sharpness constant and Eg is the energy band gap of the sample. ZnS being a direct band gap material; the value of n is ½ for the direct transition from VB to the CB [22, 33]. The band gap of ZnS and Mg–ZnS is found to be 3.15 and 3.09 eV respectively.

3.4 Photosensing study

The photosensor is an electronic component that detects the presence of visible light, infrared transmission, and/or ultraviolet (UV) energy. Mostly these are semiconductor materials having a property called photoconductivity, wherein the electrical conductance varies with the variation

in the intensity of incident illumination. It is well known that wide-bandgap semiconductors are fully sensitive to excitation light with photon energy greater than the energy bandgap. The I-V curve for ZnS and Mg–ZnS thin films were measured in the dark as well as in visible light illumination (solar simulator lamp). The device based on ZnS and Mg-doped ZnS thin films exhibit a distinct behaviour and the linearity, the curves indicate their ohmic behaviour as shown in Fig. 5a. The impact of visible light on electrical conduction indicates a very interesting result in this study. Figure 5b shows current density versus voltage (V) J-V plots of ZnS and Mg–ZnS thin film for dark condition and various illumination intensities. ZnS thin film shows a photosensitivity of ~92% and this enhanced after Mg doping to ~96% estimated using Eq. (5).

$$S\ (\%) = \frac{R_d - R_l}{R_d} \times 100 \tag{5}$$

where, S (%) Photosensitivity, R_d- resistance in dark, R_l- Resistance in light. Also, we have calculated the change in photocurrent for ZnS which were found to be 0.11 μA and 0.31 mA for Mg–ZnS thin films. Particularly, high sensitive visible light photoresponse is observed in the Mg-doped ZnS thin film which may be due to the IB observed in the UV–Vis spectra as well as in DFT results. In addition, the extraordinary photo response of Mg-doped ZnS thin films can be attributed to the better charge transfer using IB when compared to the pure ZnS thin films. IB, as an emerging technology has stimulated significant attention owing to its application in optoelectronic devices as well as an window layer in solar cells [34].

3.5 Electronic structure investigation

In order to understand the effect of Mg doping on the electronic structure of ZnS, the electronic structure calculations were performed using the DFT. The structural optimisation was first performed for wurtzite ZnS and Mg-doped ZnS. The lattice parameters of the optimized structure of ZnS and Mg–ZnS are a = 3.83 Å, c = 5.35 Å and a = 3.84 Å and c = 5.33 Å respectively. Further, the band structure of both pure and Mg-doped systems were determined and is shown in Fig. 6a, c. The band structure shows that both the systems are direct band semiconductors with an energy band gap of 1.51 eV for ZnS and 1.19 eV for Mg-doped ZnS, at the high symmetry gamma (g) point in the Brillouin zone respectively. The bandgap results reported here are close to the previous reports of wurtzite ZnS calculated using WC-GGA approximation [35]. The calculated bandstructure of Mg-doped ZnS shows IB overlapping with the CB minimum and the fermi level. This is due to the Mg incorporation in the ZnS lattice wherein the Mg act as a donor impurity [36]. The TODS shown in Fig. 6d confirms that the CB is mainly composed of Zn 4s states and the VB is dominated by s 3_p states of pure ZnS [37]. The TODS of Mg–ZnS system shows the formation of intermediate states overlapping the fermi level. These states are the 'p' states of Mg incorporated in the ZnS lattice. This further confirms the decrease in bandgap to be due to Mg doping. The presence of IB near to fermi energy results in enhanced visible light absorption as seen from the absorbance spectra and further resulted in increased photosensing properties.
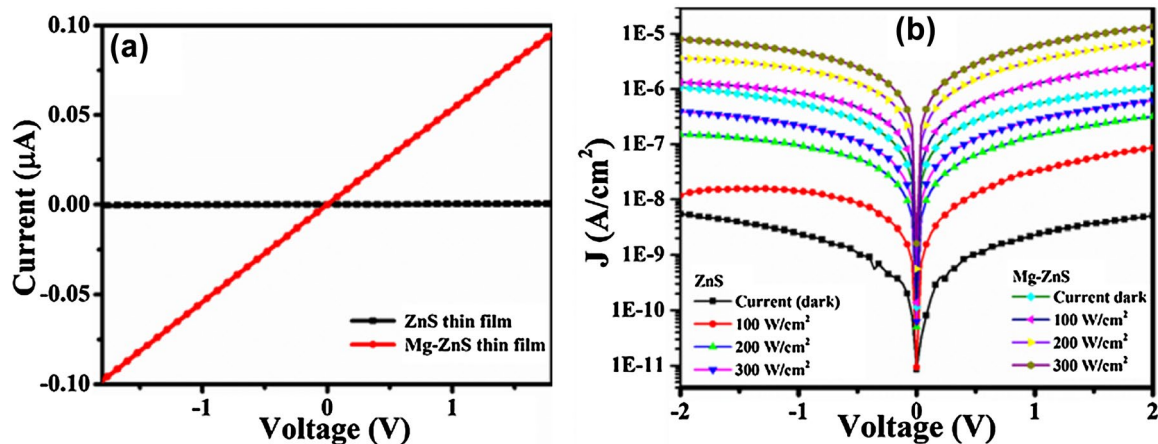

Fig. 5 **a** I-V plots of ZnS and Mg–ZnS thin films, **b** J-V plots of ZnS and Mg–ZnS thin films under dark and under illumination of 100, 200 and 300 W/cm² light
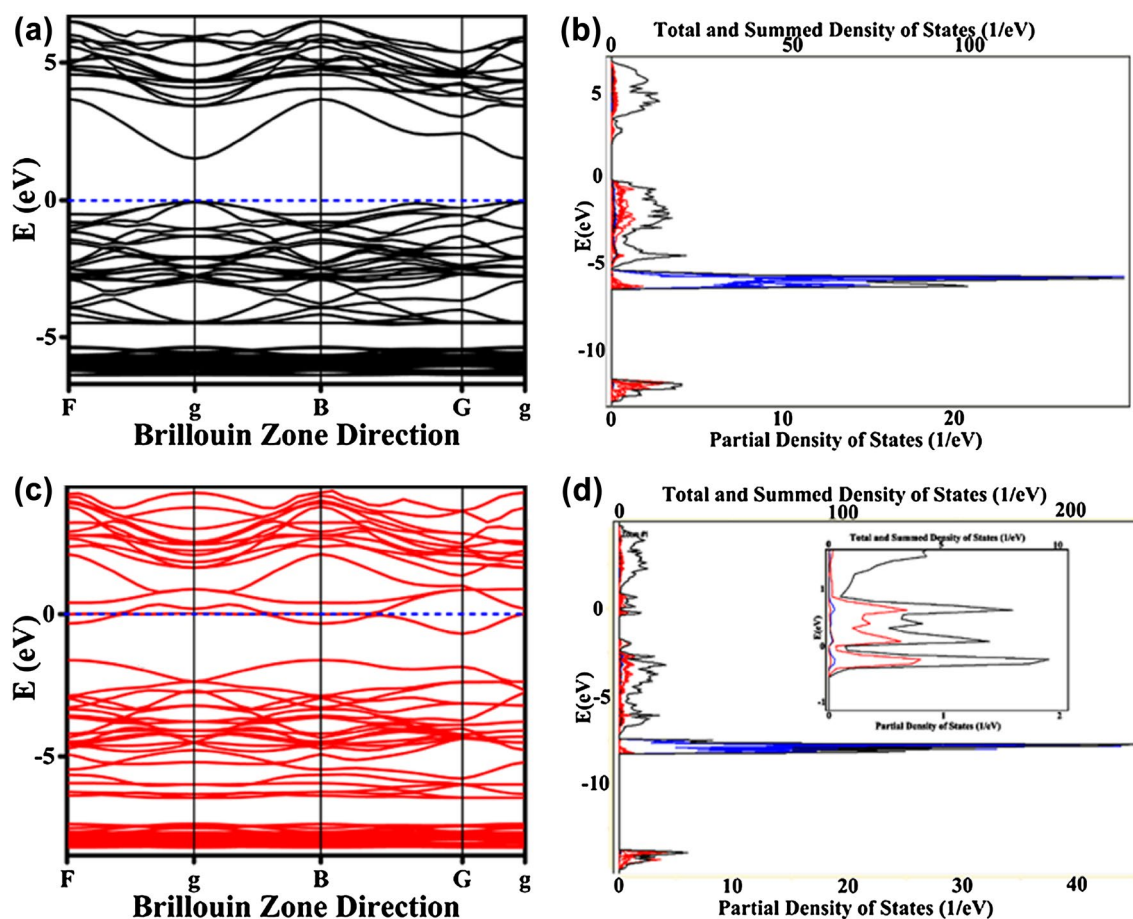
Fig. 6 Band structure of **a** ZnS, **c** Mg–ZnS and total density of states of **b** ZnS and **d** Mg–ZnS (*Inset*) zoom view of intermediate bands in Mg–ZnS TDOS

4 Conclusion

In this paper, through first-principles calculations, the structural and optoelectronic properties of wurtzite ZnS and Mg–ZnS have been studied. The theoretical calculations revealed the formation of narrow IB between the VB and the CB of the host semiconductor. These results have been correlated with the experimental results. For experimental results, the ZnS and Mg–ZnS thin films were grown on a glass substrate by simple, one step CBD method. After Mg doping, the optical absorption spectra shows an additional peak before the absorption edge for ZnS. The Mg–ZnS sample shows a slight red shift as compared to pure ZnS. Raman spectra show first order phonon modes at 356 cm^{-1} corresponding to the ZnMgS longitudinal optical phonon modes and the 435 cm^{-1} peak confirms the wurtzite crystal structure. The DFT results confirm that the Mg acts as a donor impurity, decreasing the bandgap and improving the visible light absorption. The band structure of Mg–ZnS shows the generation of IB overlapping the fermi level and the calculated TDOS of Mg–ZnS confirms

the generated IB's to be from the 'p' states of Mg. The features obtained in the electronic structure of Mg–ZnS would be used for development of next-generation optoelectronic and photovoltaic devices. The astonishing band engineering has a potential for photovoltaic, thermoelectric and optoelectronic applications.

References

1. W. Tingting, L. Xiaoguang, L. Wenjie et al., Mater. Res. Express **3**, 045905 (2016)
2. V. Nathan, A.H. Guenther, S.S. Mitra, J. Opt. Soc. Am. B **2**, 294–316 (1985)
3. A.E.-M. Aly, A. Nasr, Int. J. Photoenergy **2014**, 1–10 (2014)
4. C. Yang, M. Qin, Y. Wang, D. Wan, F. Huang, J. Lin, Sci. Rep. **3**, 1286 (2013)

5. T. Sogabe, Y. Shoji, M. Ohba et al., Sci. Rep. **4**, 4792 (2014)
6. A.S. Lin, J.D. Phillips, W.K. Metzger, Appl. Phys. Lett. **95**, 261107 (2009)
7. T. Wang, X. Li, W. Li et al., Mater. Res. Express **3**, 045905 (2016)
8. V. Popescu, G. Bester, M.C. Hanna, A.G. Norman, A. Zunger, Phys. Rev. B **78**, 205321 (2008)
9. M. Han, X. Zhang, Z. Zeng, RSC Adv. **4**, 62380–62386 (2014)
10. X. Lv, S. Yang, M. Li et al., Sol. Energy **103**, 480–487 (2014)
11. P.U. Londhe, A.B. Rohom, G.R. Bhand, S. Jadhav, M.G. Lakhe, N.B. Chaure, J. Mater. Sci. **28**, 5207–5214 (2016)
12. X. Chen, J. Jiang, Q. Liang et al., J. Mater. Chem. C **4**, 7004–7012 (2016)
13. J. Kang, W. Liu, K. Banerjee, Appl. Phys. Lett. **104**, 093106 (2014)
14. K. Usharani, A.R. Balu, J. Mater. Sci. **27**, 2071–2078 (2015)
15. K. Hoggas, C. Nouveau, A. Djelloul, M. Bououdina, Appl. Phys. A **120**, 745–755 (2015)
16. L.L. Yang, Q.X. Zhao, G.Z. Xing et al., Appl. Surf. Sci. **257**, 8629–8633 (2011)
17. I. Polat, S. Yılmaz, E. Bacaksız, Y. Atasoy, M. Tomakin, J. Mater. Sci. **25**, 3173–3178 (2014)
18. F.D. Dhlamini, V. Alberts, J. Phys. Chem. Solids **66**, 1880–1882 (2005)
19. R. Mariappan, V. Ponnuswamy, A. Chandra Bose, R. Suresh, M. Ragavendar, J. Phys. Chem. Solids **75**, 1033–1040 (2014)
20. C.V. Jagtap, V.S. Kadam, T.T. Ghogare et al., J. Mater. Sci. **27**, 12335–12339 (2016)
21. S. Kumaresan, K. Vallalperuman, S. Sathishkumar, M. Karthik, P. SivaKarthik, J. Mater. Sci. **28**, 9199–9205 (2017)
22. A.I. Inamdar, S. Lee, D. Kim et al., Thin Solid Films **537**, 36–41 (2013)
23. Z.-Y. Jiang, K.-R. Zhu, Z.-Q. Lin, S.-W. Jin, G. Li, Rare Met. 1–5 (2015). doi:10.1007/s12598-015-0505-6
24. S. Zhang, B. Yin, H. Jiang, F. Qu, A. Umar, X. Wu. Dalton Trans. **44**, 2409–2415 (2015)
25. C. Bundesmann, N. Ashkenov, M. Schubert et al., Appl. Phys. Lett. **83**, 1974 (2003)
26. X. Jiang, Y. Zhang, J. Jiang et al., J. Phys. Chem. C **116**, 22619–22624 (2012)
27. Y.M. Azhniuk, Y.I. Hutych, V.V. Lopushansky, M.V. Prymak, A.V. Gomonnai, D.R.T. Zahn, J. Phys. Chem. Solids **99**, 66–74 (2016)
28. H.K. Sadekar, N.G. Deshpande, Y.G. Gudage et al, J. Alloys Compd. **453**, 519–524 (2008)
29. D. Thapa, J. Huso, K. Miklos et al., J. Mater. Sci. **28**, 2511–2520 (2016)
30. P. Krogstrup, H.I. Jorgensen, M. Heiss et al., Nat. Photonics **7**, 306–310 (2013)
31. D.J. Desale, S. Shaikh, F. Siddiqui et al., Composites Part B **46**, 1–6 (2013)
32. U. Akgul, K. Yildiz, Y. Atici, J. Mater. Sci. **28**, 4758–4762 (2016)
33. M.Y. Shahid, M. Asghar, H.M. Arbi, M. Zafar, S.Z. Ilyas, AIP Adv. **6**, 025019 (2016)
34. M. Saadat, M. Moradi, M. Zahedifar, J. Mater. Sci. **27**, 1130–1133 (2015)
35. N. Ullah, G. Murtaza, R. Khenata, J. Rehman, H. Ud Din, S. Bin Omran, Mater. Sci. Semicond. Process. **26**, 681–689 (2014)
36. S. Kim, C.-S. Lee, S. Kim, R.B.V. Chalapathy, E.A. Al-Ammar, B.T. Ahn, Phys. Chem. Chem. Phys. **17**, 19222–19229 (2015)
37. M. Dong, P. Zhou, C. Jiang, B. Cheng, J. Yu, Chem. Phys. Lett. **668**, 1–6 (2017)